Northumbria Research Link

Northumbria University NEWCASTLE

University Library

A Highly Controlled Fabrication of Porous Anodic Aluminium Oxide Surface with Versatile Features by Spatial Thermo-anodization

Zhehui Zhang[a||], *Sreepathy Sridhar*[b||], *Guoying Wei*[a]*, *Yundan Yu*[a], *Zhongquan Zhang*[a],

Li Jiang[a], *Yumeng Yang*[a], *Muhammad Wakil Shahzad*[b], *Xue Chen*[b], *Ben B. Xu*[ab]*

[a] College of Materials & Chemistry, China Jiliang University, Hang Zhou 310018, P. R. China

[b] Department of Mechanical and Construction Engineering, Faculty of Engineering and Environment, Northumbria University, Newcastle upon Tyne, NE1 8ST, UK

[||] Authors with equal contribution.

*Corresponding Authors at: College of Materials & Chemistry, China Jiliang University, Hang Zhou 310018, P. R. China; Department of Mechanical and Construction Engineering, Faculty of Engineering and Environment, Northumbria University, Newcastle upon Tyne, NE1 8ST, UK

E-mail Address: guoyingwei@cjlu.edu.cn (G.Wei),
ben.xu@northumbria.ac.uk (Ben B. Xu).

ABSTRACT

Thermo-anodization technology has been considered as an effective means to improve the thermal, physical and chemical properties for metal alloy. In this work, we achieve a porous black layer on the surface of aluminium alloy through an environmentally friendly anodic oxidation process, with a high thermal emittance (0.96) and a high solar absorptivity (0.921). In addition, the black thermo-anodized coating layer shows a unique anti-corrosion property under UV irradiation. A hybrid hydrophobic surface has been facilitated through treating the thermo-anodized porous layer with silane. Moreover, an anti-icing feature can be realised that can effectively delay the freezing of water droplet on the surface of AA2024 aluminium alloy. As such, the specific anodic process of coating provides a simple method for improving the solar absorptivity and infrared emittance of aluminium alloys, enabling broad applications in aerospace engineering.

KEYWORDS: Anodic oxidation; Solar absorptivity; Emittance; Surface wetting; Anti-freezing

1. Introduction

Controllable thermo-anodized coating (CTC) with a passive and effective protection to a spacecraft, has attracted considerable research interests in recent years [1-3]. Such coatings have been widely used in the electronic housing packages of spacecraft with black CTC on the alloys, to fulfil high solar absorptivity and high emittance. Recently, the demand of these coatings climbs in response to the growing applications in aerospace engineering[4-9], where the common technical focuses are to develop CTC surfaces with resistance against corrosion[10] and icing[11], as well as high solar absorptivity (a_s)[12] and thermal emittance (ε)[13]. Some mechanisms have been proposed to achieve controlled oxidation on alloys[14] and Plasma Electrolytic Oxidation (PEO)[15]. Yao *et al* prepared a black high-solar-absorptivity and high-emittance coating on Titanium alloy with a a_s of 0.93 and ε of 0.88[16]. Shang *et al* used micro-arc oxidation to prepare a multi-layered GO coated Magnesium alloy with an improved corrosion resistance[17]. While the coating technology on the surfaces of Titanium and Magnesium alloys advances[18-20], their anti-corrosion performance declines at the presence of solar light[21-24]. Anodic aluminium alloys manufactured via traditional anodization methods exhibits mild anti-corrosion behaviour with reduced solar absorptivity and thermal emittance[25-27]. Hence, a conventional process to achieve high performance CTC coated Aluminium alloy has not been exploited elsewhere.

In this paper, we propose a conventional CTC strategy on the surface of aluminium alloys. The combination of anodic current density and temperature accelerate the anodization process without the need for involvement of changes to electrolyte concentration and provide controllability over the porous structure formation on the anodized aluminium oxide surface [28]. The as-prepared coating layer presents an excellent property with both absorptivity and emittance values above 0.9. The surface microstructure of coating layer can be adjusted by changing the

anodizing temperature and current density. The fabricated black CTC possess a unique anti-corrosion property under UV irradiation. By constructing a hybrid layer with a silanization process, an improved anti-icing property can be facilitated by delaying the frozen time for the water droplet on the surface of AA2024 aluminium alloy.

2. Experimental Section

2.1. Materials and fabrication of black CTC layer. A sample slice of AA2024 aluminium alloy (40 mm × 40 mm × 2 mm) was purchased from AA(Guangzhou) Materials Co Ltd. In the first step, it was mechanically polished by SiC sand papers (from grit #1000 to #2500) to reduce the surface roughness and improve the reflectance. In the second step, it was etched in 1 mol/L NaOH for 12 min and rinsed by deionized (DI) water to remove contaminants. At last, the samples were cleaned in a dilute sulfuric acid solution (1 mol/L) for 2~3 min and rinsed again with DI water. The anodic parameters and components of anodization solution are given in the following table.

Table 1. The electrolyte composition and processing parameters for anodization process

H_2SO_4 (g/L)	$H_2C_2O_4$ (g/L)	$C_4H_6O_5$ (g/L)	$Fe_2(SO_4)_3$ (g/L)	T °C	I (A/dm^2)	Time (min)
30	40	30	6	0	3-7	60
30	40	30	6	0-10	5	60

2.2. Characterization. The composition of anodized coating layer was examined by the X-ray diffractometer technique (Shimadzu, LabX XRD-6100). The microstructure of coating was analysed by scanning electron microscope (FE-SEM, HITACHI-SU8010). The thickness was measured under an inverted reflected light microscope (GX51, OLYMPUS). The surface roughness was evaluated by a surface roughness measuring device (S1910DX3, KLA-TENCOR).

Potentiodynamic electrochemical measurement was performed to characterize the anti-corrosion property. The testing solution consisted of DI water and reagent-grade NaCl (3.5 wt. %) in order to simulate the seawater environment, with a sample area of 1 cm^2 exposed to the solution. The electrochemical tests were conducted by employing the potentiodynamic polarisation method in a conventional three-electrode cell. The CTC alloy, a platinum foil, and a saturated calomel electrode (SCE) were used as working, counter, and reference electrodes, respectively. The polarization curves were obtained using the PARSTAT 2273 Workstation, with the 3.5 wt. % NaCl solution filled electrochemical cell after UV irradiation at a wavelength of 400 nm.

2.3. The solar absorptivity and emittance measurement. The solar absorptivity of coating was assessed by a UV-3600 spectrophotometer at a range of 200–800 nm. The emittance was measured by IR-2 dual-band emittance scope (Shanghai Chengbo) under the range of 8–16 μm at room temperature. The solar absorptivity α_s was calculated using the following equation:

$$\alpha_S = 1 - \rho_S = \frac{\int_{\lambda_2}^{\lambda_1} \rho_\lambda S_\lambda d\lambda}{\int_{\lambda_2}^{\lambda_1} \rho_\lambda d\lambda} \tag{1}$$

where λ is the wavelength, ρ_S is the reflectance and S_λ is the solar radiation spectrum. For a thin coating, the analytical expression of spectral absorptivity $\alpha(\lambda)$ of coating can be obtained as:

$$\alpha(\lambda) = (1 - \rho_c(\lambda)) - \frac{\rho_b(\lambda)(1-\rho_c(\lambda))^2}{\exp\left(\frac{16\pi kd}{\lambda}\right) - \rho_c(\lambda)\rho_b(\lambda)} \tag{2}$$

where $\rho_b(\lambda)$ is the substrate reflectance, $\rho_c(\lambda)$ is the coating reflectance, d is the coating thickness and k is the coating extinction coefficient.

2.4 Surface wettability assessment. The CTC layer was treated by silane, then annealed at certain temperatures. Water contact angle (CA) was measured with an OCA-20 instrument (DataPhysics GmbH, Germany) at room temperature. The anti-icing property of the prepared superhydrophobic surface was evaluated by placing it on a cooling stage at a temperature of - 8°C and depositing a water droplet of 10 μL on the sample surface.

3. Results and Discussion

3.1. Realization of thermo-anodized structural layer on the surface of aluminum

The thermo-anodization process (**Fig. 1a-1b**) was performed by utilizing an AA2024 alloy sample as anode and a pure aluminium slice as cathode. By comparing the surface morphology and polarization curves for the sample fabricated under different anodization duration (**Fig. S1**), the coating layer show a decaying trend if the processing time exceeds 60 min due to the increasing rate of the anodic oxide coating dissolution. Thus, a processing time of 60 min was selected for the rest of study. We focus on the effects of anodizing conditions (i.e. temperature and current density) on microstructure (thickness, surface roughness and porosity, **Fig. 1b**), where the microstructure is anticipated to be tuned with the dependencies on the current density and/or the anodizing temperature [29-32].

The SEM observation (**Fig. 1c-1e**) suggests a controllable formation of surface morphology under thermo-oxidization with a uniform distribution of porous surface around 20 nm in pore diameter at a current density of 5 A/dm^2 and temperature of 10°C. There is an interesting presence of wavy structures in **Fig. 1d**, due to the break in equilibrium of a pristine coating layer before the growth of porous structure is initiated. Further analysis from AFM profiling (**Fig. 1f-1h**) identifies the increase in surface roughness when the pore structure is developed, which is in a good agreement with SEM results. When the current density increases (**Fig. S2**), the thermal effect accelerates the mobility of OH$^-$ in electrolyte, leading to the dissolution of solid layer and an increment in the pore size[33,34]. XRD results in **Fig. S3a**, show a broad, bread-shaped peak in the range of 15°~ 30°, which may be affiliated with the amorphous alumina. Other sharp diffraction peaks correspond to those from the γ-Al$_2$O$_3$. As shown in **Fig. S3c**, **S3f** – **S3h**, an increasing average pore size (from 10 nm to 16 nm) is discovered when the anodizing temperature increases

from 0 °C to 10 °C. The appearance of black surface is caused by the formation of magnetite Fe_3O_4 which is validated from the XPS analysis and resulted in binding energy at 284.6 eV with an indefinite carbon C1s. The results in **Fig. S4a** show C, O and Fe elements on the surface of anodic coatings, and **Fig. S4b** shows the binding energy of Fe 2p, which can be divided into two different components, representing two different oxidation states for iron in the coatings, i.e. Fe^{2+} at 710.4 and 724.1 eV, Fe^{3+} at 712.3 and 726.1 eV. The peaks relate to 2p3/2 and 2p1/2 signals of octahedral Fe^{2+}, Fe^{3+} and tetrahedral Fe^{3+}, respectively, which further confirms the existence of Fe_3O_4.

In **Fig. 1i**, the increase in anodization current density drives the ion exchange rate higher within the barrier, and increases the thickness (115 μm) and roughness of coating layer (1.6 μm) at a current density of 7 A/dm^2, wherein the reaction efficiency seems to reach the peak since the anodization equilibrium was supported by the local components of anodization along with sustainable mass transportation in solution. However, further increase in the anodization current density promote pronounced dissolution rate compared to oxide growth rate and the oxide thickness begins to decrease (**Fig. 1i**). In **Fig. 1j**, both coating thickness and roughness decrease when the anodizing temperature (T) increases. The maximum thickness (103 μm) is obtained at $T = 0$ °C, with a maximum roughness (~ 2 μm) at $T = 5$ °C. While the increased dissolution rate at higher temperature encourages the removal of residuals leading to a reduction on surface roughness [35], the elevating temperature also accelerates the dissolution of anodized coating (i.e. coating layer) to decrease the thickness. The average pore size *vs* anodic current density in **Fig S5** unveils the trend when tuning the anodization current density and temperature. It should be noted that the surface becomes rougher and achieves inhomogeneity when e either of the anodization current density or temperature is increased.

3.2. Evaluations of solar absorption and emittance

We then investigate the solar absorptivity and emittance performances for the CTC layers. In **Fig. 2a**, the reflectance of coating layer decreases gradually when the current density increases from 1 A/ dm^2 to 3 A/ dm^2. When the current density reaches above 1 A/dm^2, the reflectance value drops due to the intensive growth of anodized layer (**Fig. S3b**), which breaks the equilibrium to nucleate pristine oxidized coating layer. When the current density further increases above 3 A/dm^2 (**Fig. S3d**), the uniform growth of porous structure can be established to increase the reflectance. It is notable that the coating reflectance increase as temperature elevates (**Fig. 2b)** at a fixed current density of 5 A/ dm^2, indicating that a higher temperature is thermodynamically favourable to create the anodization equilibrium. However, cracking likely to occur on the coating film (**Fig. 2c)** at a higher temperature (8°C or above), due to the localized stress during the intensive growth of layer. Hence, a combination usage of temperature and current density can fulfil a highly controlled surface roughness with superior reflectance characteristics.

The solar absorptivity (α_s) and emittance (ε) for the anodized surfaces under different processing conditions are summarized in **Fig. 2d-2e**. A set of absorptance (α_s) values are obtained as 0.673, 0.897, 0.921, 0.881, 0.845, at a various current density setting from 1 A/dm^2 to 9 A/dm^2, respectively. Compared with the smooth untreated aluminium alloy surface with an absorptivity of 0.557 and an emittance of 0.16, significant enhancements are achieved with an absorptivity of 0.921 and an emittance of 0.96 for the anodized layer. When the anodizing temperature increases (**Fig. 2e**), the solar absorptivity shows a decreasing trend from a value of 0.921 at 0 °C, to a value of 0.862 at 10 °C. By plotting the absorptivity and emittance as a function of coating thickness (**Fig. 2f**), both absorptivity and emittance increase when the thickness increases initially, then reaches a plateau at around 50 µm. Our hypothesis is that the surface homogeneity at around 50

μm provides the best absorbing feature. Detailed 3D profiling on porous morphology (including film qualities and structures) would be a direct evidence to support this point, however, the challenge in instrumentation remains in exploring the 3D porous morphology at this moment, therefore, we defer this part of investigation to the future work.
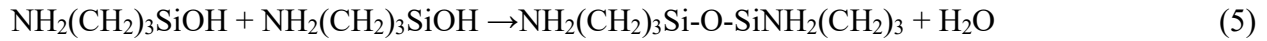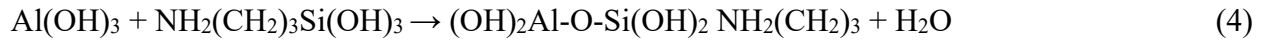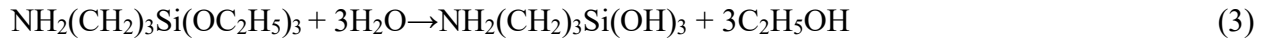
3.3. Corrosion resistance of black coated aluminium alloys under UV radiation

We next characterize the CTC coating layer under UV irradiation (400 nm). Prior to the UV irradiation, the potentiodynamic polarization curves are benchmarked in **Fig. 3a** and **3c**, where the best coating corrosion resistance appears with a maximum corrosion current density and a self-corrosion potential of 1.148E-5 A/cm^2 and -0.545 V at a current density of 5 A/dm^2 under 0 °C. After UV irradiation, the potentiodynamic polarization curves (**Fig. 3b** and **3d**) suggest limited changes on the overall corrosion current density. For the CTC layer fabricated at an optimal state with a current density of 5 A/dm^2 and a temperature of 0 °C, the surface achieved a maximum corrosion current density value of 1.659E-5 A/cm^2 and a self-corrosion potential of -0.565 V, which shows an effective UV shielding feature for the CTC layer. This improvement is attributed to an accelerated rate of dissolution of ions, leading to initiation of corrosion/pitted surface when the temperature and anodic current density increase.

3.4. Silane assisted superhydrophobicity and validation of characteristics

One of the essential criteria for a coating technology to be used in aerospace engineering, is the surface icephobicity[36-40]. Alongside with the recent anti-icing perspectives by using heated surface[41], textured surfaces[42-45], latest approach of liquid infused surface present a low cost and programmable strategy to distinguish itself from above[46-48]. Here, we develop a hybrid strategy by applying a silanization layer to seal the anodized porous surface (**Fig. 4a**), via a

hydrolysis reaction (**Fig. S6**), where the silanol groups react with the hydroxides to generate strong Si-O-Me metal bonds. The silane reaction on the surface imparts the necessary hydrophobic character due to the controllability over interpore distance present on the thermo-anodized aluminium oxide surface by providing more contact area between liquid impregnated surface (Wenzel state)[49]. Such Si-O-Me network is expected to collaboratively work with the anodized porous surface to provide a robust superhydrophobicity to prevent the penetration of corrosive solution (**Fig. 4b**). The above reactions are illustrated as following:

$$NH_2(CH_2)_3Si(OC_2H_5)_3 + 3H_2O \rightarrow NH_2(CH_2)_3Si(OH)_3 + 3C_2H_5OH \tag{3}$$

$$Al(OH)_3 + NH_2(CH_2)_3Si(OH)_3 \rightarrow (OH)_2Al\text{-}O\text{-}Si(OH)_2\ NH_2(CH_2)_3 + H_2O \tag{4}$$

$$NH_2(CH_2)_3SiOH + NH_2(CH_2)_3SiOH \rightarrow NH_2(CH_2)_3Si\text{-}O\text{-}SiNH_2(CH_2)_3 + H_2O \tag{5}$$

The optimal surface is achieved at an annealing temperature of 30 °C (**Fig. 4c**), where the surface roughness result shows a small value of 930 nm with no obvious changes on overall coating thickness. The reflectance result (**Fig. 4d**) also reveals limited changes with stable plateau values due to the well-maintained thickness. While the emissivity results can be measured, the solar absorptance values are calculated from following equation, $\alpha_s = 1 - \rho_S = \int_{\lambda 1 \lambda 2} \rho_\lambda S_\lambda d\lambda / \int_{\lambda 1 \lambda 2} \rho_\lambda d\lambda$, where ρ_S is the reflectance of coating and S_λ is the solar radiation spectrum. An emittance peak value (0.975) is obtained at a hydrolysis temperature of 50 °C (**Fig. 4e**), while the absorptance remains almost unchanged. Considering the diameter of pores between 10-50 nm (**Fig. S7**), the light, whose wavelength is normally in hundreds of nanometres, is too large to enter the oxide layer pores caused by uneven roughness on the surface. Hence, the surface roughness should be considered before annealing silane on the surface to determine a superior emittance and absorptance characteristics.

3.5. Anti-icing performance

The resistance of water residual onto the silane coated porous anodic aluminium oxide layer can delay the formation of ice, which can be explained by the hypothesised wenzel to cassie-baxter transition (**Fig. 5a**). In **Fig. 5b-5e**, contact angle (CA) results demonstrate the shifting of CA value from 74º at an annealing temperature of 20 °C, to 134.5º when the silane layer is annealed at 40 °C. For the porous alumina surface without silane layer, a contact angle of less than 60° is obtained due to the impregnation of water droplet within the porous surface which present a typical hydrophilic state. When the porous aluminium surface is incubated with silane layer at a low temperature, a moderately increasing CA of 80° is appeared indicating a full wenzel or near-wenzel intermediate state on the surface. When the surface is further incubated at a higher annealing temperature of 30°C, a strong adhesion between silane coating and the anodic surface is facilitated with an apparent CA of 125°, which show a complete or near-cassie intermediate state. A programmable surface wetting state can be realised by varying the annealing temperature of silane coating, to induce the transition between Wenzel to Cassie state.

Du *et al* [50] reported the ineffective performance for the sole Si-O-Me network on flat aluminium to resist the icing of water, however, the Si-O-Me network on porous anodized surface in our study remains hydrophobic after immersing in water for 100 hours (CA ~ 119º ± 9º), and exhibited robustness (~ 15º decrease in static CA) after 50 rounds of icing tests, as shown in **Fig. S8**. The summary of CA and contact angle hysteresis (CAH) in **Fig. 5f** shows that the surface is mostly hydrophobic and has the lowest CAH value at an annealing temperature of 40 °C. It should be noted that the CA value decreases with an annealing temperature of 50 °C, which agrees with the rise in roughness in **Fig. 5c**, because of the breaking of thermal dynamic equilibrium at a high temperature, yielding an early termination of reaction to generate uniform surface silane network.

The patchy surface is likely to cast negative impact on the initiation of homogeneous *Si-O-Me* network, thus reducing the overall surface hydrophobicity. The icephobic measurement was performed on the surfaces of untreated CTC coating (**Fig. 5g**) and hybrid CTC surface at an annealing temperature of 40 °C (**Fig. 5i**). From **Fig. 5g-5j**, the icing process takes 15 sec for hybrid surface, which is 150% of the time on untreated surface (10 sec) and demonstrates an improvement in the anti-icing function for the hybrid surface. However, the overall anti-icing performance still needs be improved since the icing time remains rather short, compared with a variety of existing researches. But the improvement presented in this study point out a research direction which we will investigate intensively in future.

4. Conclusions

A high-performance CTC coating technology is described by thermo-anodizing the surface of aluminium alloy to achieve a black coating layer with an emittance of 0.96 and an absorptivity of 0.921. By tuning the coating parameters, an optimized coating condition is achieved at the current density of 5 A/dm^2 and anodizing temperature of 0 °C. Moreover, the CTC coating present a good resistance to UV irradiation, which enables an UV shielding effect for the emerging applications in civil and aerospace engineering. By further constructing a hybrid layer via creating a silane layer to seal the CTC surface, a hydrophobic coating can be facilitated with anti-icing feature that can delay the freezing of water droplet on the surface of AA2024 aluminium alloy. This thermo-anodization strategy is expected to advance the coating technology towards future aerospace engineering.

Associated Content

Author Contribution Statement

Guoying Wei (G.Y.W.) and Ben Bin Xu (B.B.X.) managed the overall programme. Zhehui Zhang (Z.H.Z.), Yundan Yu (Y.D.Y.) and Zhongquan Zhang (Z.Q.Z) completed experimental work, Z.H.Z. and Sreepathy Sridhar(S.S.) performed the data analysis. G.Y.W., B.B.X., S.S. and Z.H.Z. drafted the manuscript together, with the contributions from Li Jiang (L.J.), Yumeng Yang(Y.M.Y.) and Muhammad Shahzad (M.S).

Conflicts of Interest

There are no conflicts to declare.

References

[1] W. Lee, S.J. Park, Porous anodic aluminum oxide: anodization and templated synthesis of functional nanostructures, Chem. Rev. 114(2014) 7487-7556. https://doi.org/10.1021/cr500002z.

[2] M. Holynska, A. Tighe, C. Semprimoschnig, C. Coatings and thin films for spacecraft thermo-optical and related functional applications, Adv. Mater. Inter. 5(2018) 1-20. https://doi.org/10.1002/admi.201701644.

[3] M. Pashchanka, Multilevel self-organization on anodized aluminium: discovering hierarchical honeycomb structures from nanometre to sub-millimetre scale, Phys. Chem. Chem. Phys. 22(2020) 15867-15875. https://doi.org/10.1039/D0CP01717E.

[4] J. Lee, D. Kim, C.H. Choi, W. Chung, Nanoporous anodic alumina oxide layer and its sealing for the enhancement of radiative heat dissipation of aluminum alloy, Nano Energy 31(2017) 504-513. https://doi.org/10.1016/j.nanoen.2016.12.007.

[5] M. Zhou, T. Lin, F. Huang, Y. Zhong, Y. Wang, Y. Tang, H. Bi, D. Wang, J. Lin, Highly conductive porous graphene/ceramic composites for heat transfer and thermal energy storage, Adv. Func. Mater. 23(2013) 1-7. https://doi.org/10.1002/adfm.201202638.

[6] W.M. Seidl, M. Bartosik, S. Kolozsvári, H. Bolvardi, P.H. Mayrhofer, Improved mechanical properties, thermal stabilities, and oxidation resistance of arc evaporated Ti-Al-N coatings through alloying with Ta, Surf. Coatings Technol. 344 (2018) 244–249, https://doi.org/10.1016/j.surfcoat.2018.03.014.

[7] S. Shin, Q. Wang, J. Luo, R. Chen, Advanced materials for high-temperature thermal transport, Adv. Func. Mater. 30(2020) 1-23. https://doi.org/10.1002/adfm.201904815.

[8] Y. Zhu, K. Cao, M. Chen, L. Wu, Synthesis of UV-responsive self-healing microcapsules and their potential applications in aerospace coatings, ACS Appl. Mater. Interfaces 11(2019) 33314-33322. https://doi.org/10.1021/acsami.9b10737.

[9] M. Odarczenko, D. Thakare, W. Li, S.P. Venkateswaran, N.R. Sottos, S.R. White, Sunligh-activated self-healing polymer coatings, Adv. Energ. Mater. 22(2019) 1901223- 1901238. https://doi.org/10.1002/adem.201901223

[10] F. Khelifa, S. Ershov, M.E. Druart, Y. Habibi, D. Chicot, M.G. Oliver, R. Snyders, P. Dubois, A multilayer coating with optimized properties for corrosion protection of Al, J. Mater. Chem. A. 3(2015) 15977-15985. https://doi.org/10.1039/C5TA01920F.

[11] S. Brown, J. Lengaigne, N. Sharifi, M. Pugh, C. Moreau, A. Dolatabadi, L. Martinu, J.E. Klemberg-Sapieha, Durability of superhydrophobic duplex coating systems for aerospace applications, Surf. Coatings Technol. 401(2020) 1264249. https://doi.org/10.1016/j.surfcoat.2020.126249.

[12] M. Chen, J. Mandal, Q. Ye, Q. Cheng, T. Gong, T. Jin, Y. He, N. Yu, Y. Yang, A scalable dealloying technique to create thermally stable plasmonic nickel selective solar absorbers, ACS Appl. Energ. Mater. 2(2019) 6551-6557. https://doi.org/10.1021/acsaem.9b01112.

[13] M. Farhat, T.C. Cheng, K.Q. Le, M.M.C. Cheng, H. Bagci, P.Y. Chen, Mirror-black dark alumina: A nearly perfect absorber for thermoelectronics and thermophotovoltaics, Sci. Rep. 6(2016) 1-11. https://doi.org/10.1038/srep19984.

[14] F. Peng, D. Wang, Y. Tian, H. Cao, Y. Qiao, X. Liu, Sealing the pores of PEO coating with Mg-Al layered double hydroxide: Enhanced corrosion resistance, cytocompatibility and drug delivery ability, Sci. Rep. 7(2017) 1-12. https://doi.org/10.1038/s41598-017-08238-w.

[15] H. Niazi, F. Golestani-Fard, W. Wang, M. Shahmiri, H.R. Zargar, A. Alfantazi, R. Bayati, Structure-property correlation in EEMAO fabricated TiO_2-Al_2O_3 nanocomposite coatings, ACS Appl. Mater. Interfaces 6(2014) 5538-5547. https://doi.org/10.1021/am405938n.

[16] Z. Yao, Q. Xia, P. Ju, J. Wang, P. Su, D. Li, Z. Jiang, Investigation of absorptance and emissivity of thermal control coatings on Mg-Li alloys and OES analysis during PEO process, Sci. Rep. 6(2016) 1-9. 10.1038/srep29563.

[17] W. Shang, F. Wu, Y. Wang, A.R. Baboukani, Y. Wen, J. Jiang, Corrosion resistance of micro-arc oxidation/graphene oxide composite coating on magnesium alloys, ACS Omega 5(2020) 7262-7270. https://doi.org/10.1021/acsomega.9b04060.

[18] L.Y. Cui, R.C. Zeng, S.K. Guan, W.C. Qi, F.Zhang, S.Q. Li, E.H. Han, Degradation mechanism of micro-arc oxidation coatings on biodegradable Mg-Ca alloys: The influence of porosity, J. Alloys Compd. 695 (2017) 2464-2476. 10.1016/j.jallcom.2016.11.146.

[19] R.F. Zhang, S.F. Zhang. Formation of micro-arc oxidation coatings on AZ91HP magnesium alloys, Corr. Sci. 51(2009) 2820-2825. https://doi.org/10.1016/j.corsci.2009.08.009.

[20] R.F. Zhang, S.F. Zhang, J.H. Xiang, L.H. Zhang, Y.Q. Zhang, S.B. Guo, Influence of sodium silicate concentration on properties of micro arc oxidation coatings formed on AZ91HP magnesium alloys, Surf. Coatings Technol. 206(2012) 5072-5076. https://doi.org/10.1016/j.surfcoat.2012.06.018.

[21] Z. Yao, Q. Shen, A. Niu, B. Hu, Z. Jiang, Preparation of high emissivity and low absorbance thermal control coatings on Ti alloys by plasma electrolytic oxidation, Surf. Coatings Technol. 242(2014) 146-151. https://doi.org/10.1016/j.surfcoat.2014.01.034.

[22] Z. Yao, Q. Xia, Q. Shen, P. Ju, P. Su, B. Hu, Z. Jiang, A facile preparation of ceramic coatings on Ti alloys for thermal protection systems, Sol. Energ. Mat. Sol. C 269(2015) 220-227. https://doi.org/10.1016/j.solmat.2015.07.009.

[23] T. Wang, J. Du, S. Ye, L. Tan, J.J. Fu, Triple-stimuli-responsive smart nanocontainers enhanced self-healing anticorrosion coatings for protection of aluminum alloy, ACS Appl. Mater. Interfaces 11(2019) 4425-4438. https://doi.org/10.1021/acsami.8b19950.

[24] A. Barulin, J.B. Claude, S. Patra, A. Moreau, J. Lumeau, J. Wenger, Preventing aluminum photocorrosion for ultraviolet plasmonics. J. Phys. Chem. Lett. 10(2019) 5700-5707. 10.1021/acs.jpclett.9b02137.

[25] M.A. Amim, Uniform and pitting corrosion events induced by SCN⁻ anions on Al alloys surfaces and the effect of UV light, Electrochimica Acta 56(2011) 2518-2531. https://doi.org/10.1016/j.electacta.2010.12.045

[26] C. Zhang, W. Li, D. Yu, Y. Wang, M. Yin, H. Wang, Y. Song, X. Zhu, P. Chang, X. Chen, D. Li, Wafer-scale highly ordered anodic aluminum oxide by soft nanoimprinting lithography for optoelectronics light management, Adv. Mater. Interfaces 4(2017) 1-7. https://doi.org/10.1002/admi.201601116.

[27] C. Jeong, J. Lee, K. Sheppard, C.H. Choi, Air-impregnated nanoporous anodic aluminum oxides for enhancing the corrosion resistance of aluminum, Langmuir 31(2015) 11040-11050. https://doi.org/10.1021/acs.langmuir.5b02392.

[28] W. Lee, R. Ji, U. Gösele, K. Nielsch, Fast fabrication of long-range ordered porous alumina membranes by hard anodization, Nat. Mater. 5 (2006) 741–747. https://doi.org/10.1038/nmat1717.

[29] L. Bruschi, G. Mistura, P.T.M. Nguyen, D.D. Do, D. Nicholson S.J. Park, W. Lee, Adsorption in alumina pores open at one and at both ends, Nanoscale 7(2015) 2587-2596. 10.1039/C4NR06469K.

[30] N.A. Vinogradov, G.S. Harlow, F. Carla, J. Evertsson, L. Rullik, W. Linpe, R. Felici, E. Lundgren, Observation of pore growth and self-organization in anodic alumina, ACS Appl. Nano Mater. 1(2018) 1265-1271. https://doi.org/10.1021/acsanm.7b00303.

[31] H. Liu, W. Lin, Z. Lin, L. Ji, M. Hong, Self-organized periodic microholes array formation on aluminum surface via femtosecond laser ablation induced effect, Adv Func Mater 29(2019) 1-7. https://doi.org/10.1002/adfm.201903576.

[32] B. Wang, W. Guo, Y. Fu, Anodized aluminum oxide separators with aligned channels for high-performance Li-S batteries. ACS Appl. Mater. Interfaces 12(2020) 5831-5837. https://doi.org/10.1021/acsami.9b19196.

[33] Y. Yan, Z. Xu, C. Liu, H. Dou, Z. Wei, J. Ma, Q. Dong, H. Xu, Y. He, Z. Ma, X. Yang, Rational design of the robust Janus shell on silicon anodes for high-performance lithium-ion batteries, ACS Appl. Mater. Interfaces 11(2019) 17375-17383. https://doi.org/10.1021/acsami.9b01909.

[34] T. Zelovich, L. Vogt-Maranto, M.A. Hickner, S.J. Paddison, C. Bae, D.R. Dekel, M.E. Tuckerman, Hydroxide ion diffusion in anion-exchange membranes at low hydration: Insights from Ab initio molecular dynamics, Chem. Mater. 31(2019) 5778-5787. https://doi.org/10.1021/acs.chemmater.9b01824.

[35] A.S. Esmaeily, S. Mills, J.M.D. Coey, Exceptional room-temperature plasticity in amorphous alumina nanotubes fabricated by magnetic hard anodization, Nanoscale 9(2017) 5205-5211. 10.1039/C7NR00095B.

[36] S. Jung, M. Dorrestjin, D. Raps, A. Das, C.M. Megaridis, D. Poulikakos, Are superhydrophobic surfaces best for icephobicity? Langmuir 27(2011) 3059-3066. https://doi.org/10.1021/la104762g.

[37] Y.H. Ng, S.W. Tay, L. Hong, Formation of icephobic surface with micron-scaled hydrophobic heterogeneity on polyurethane aerospace coating, ACS Appl. Mater. Interfaces 10(2018) 37517-37528. https://doi.org/10.1021/acsami.8b13403.

[38] X. Huang, N. Tepylo, V. Pommier-Bidinger, M. Budinger, E. Bonaccurso, P. Villedieu, L. Bennani, A survey of icephobic coatings and their potential use in a hybrid coating/active ice protection system for aerospace application, Prog. Aerosp. Sci. 105(2019) 74-97. https://doi.org/10.1016/j.paerosci.2019.01.002.

[39] V. Vercillo, S. Tonnichia, J.M. Romano, A. Garcia-Giron, A.I. Aguillar-Morales, S. Alamri, S.S. Dimov, T. Kunze, A.F. Lasagni, E. Bonaccurso, Design rules for laser-treated metallic surfaces for aeronautic applications, Adv. Func. Mater. 30(2020) 1-12. https://doi.org/10.1002/adfm.201910268.

[40] M.J. Kreder, J.P. Alvarenga, J. Aizenberg, Design of anti-icing surfaces: smooth, textured or slippery, Nat. Rev. Mater. 1(2016) 15003. https://doi.org/10.1038/natrevmats.2015.3.

[41] L.E. Dodd, D. Wood, N.R. Geraldi, G.G. Wells, G. McHale, B.B. Xu, S. Stuart-Cole, J. Martin, M.I. Newton, Low friction droplet transportation on a substrate with a selective leidenfrost effect, ACS Appl. Mater. Interfaces 8(2016) 22658-22663. https://doi.org/10.1021/acsami.6b06738.

[42] L. Mischenko, B. Hatton, V. Bahadur, J.A. Taylor, T. Krupenkin, J. Aizenberg, Design of ice-free nanostructured surfaces based on repulsion of impacting water droplets, ACS Nano 4(2010) 7699-7707. https://doi.org/10.1021/nn102557p.

[42] C. Jeong, C.H. Choi, Single-step direct fabrication of pillar-on-pore hybrid nanostructures in anodizing aluminum for superhydrophobic efficiency, ACS Appl. Mater. Interfaces 4(2012) 842-848. https://doi.org/10.1021/am201514n.

[44] L. Li, T. Huang, J. Lei, J. He, L. Qu, P. Huang, W. Zhou, N. Li, F. Pan, Robust biomimetic-structural superhydrophobic surface on aluminum alloy, ACS Appl. Mater. Interfaces 7(2015) 1449-1457. https://doi.org/10.1021/am505582j.

[45] A. Gauthier, S. Symon, C. Clanet, D. Quere, Water impacting on superhydrophobic macrotextures, Nat. Comm. 6(2015) 1-6. 10.1038/ncomms9001.

[46] Z. Li, Y. Liu, M. Lei, A. Sun, S. Sridhar, Y. Li, X. Liu, H. Lu, Y.Q. Fu, B.B. Xu, Stimuli-responsive gel impregnated surface with switchable lipophilic/oleophobic properties, Soft Matter 16(2020) 1636-1641. https://doi.org/10.1039/C9SM02016K.

[47] P. Baumli, H. Teisala, H. Bauer, D. Garcia-Gonzalez, V. Damle, F. Geyer, M. D'Acunzi, A. Kaltbeitzel, H.J. Butt, D. Vollmer, Flow-induced long-term stable slippery surfaces, Adv. Sci. 6(2019) 1-8. https://doi.org/10.1002/advs.201900019.

[48] P. Kim, T.S. Wong, J. Alvarenga, M.J. Kreder, W.E. Adorno-Martinez, J. Aizenberg, Liquid-infused nanostructured surface with extreme anti-ice and anti-frost performance, ACS Nano 6(2012) 6569-6577. https://doi.org/10.1021/nn302310q.

[49] J. G. Buijnsters, R. Zhong, N. Tsyntsaru, J.-P. Celis, Surface wettability of macroporous anodized aluminium oxide, ACS Appl. Mater. Interfaces 5(2013) 3224-3233. https://doi.org/10.1021/am4001425

[50] S.A. Kulinich, M. Honda, A.L. Zhu, A.G. Rozhinb, X.W. Du, The icephobic performance of alkyl-grafted aluminum surfaces, Soft Matter 11(2015) 856-861.
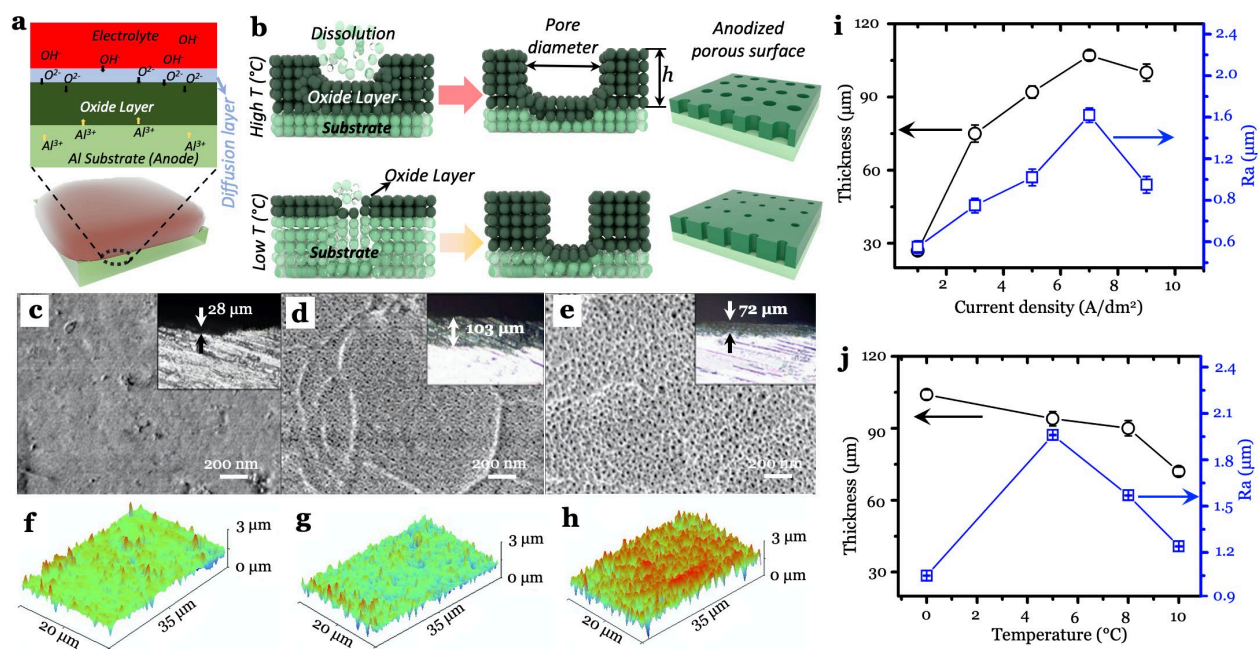
Fig. 1 Schematic illustrations of (a) anodic oxidation mechanism and (b) formation of porous surface layer on aluminium alloy during the thermo-anodization. SEM observations of surface morphology for coatings at (c) 1 A/dm^2, 0°C; (d) 5 A/dm^2, 0°C; (e) 5 A/dm^2, 10°C. AFM profiles for the surfaces fabricated at (f) 1 A/dm^2, 0°C; (g) 5 A/dm^2, 0°C; (h) 5 A/dm^2, 10°C. Coating thickness and roughness results as a function of (i) oxidization current density at a fixed temperature of 0 °C, and (j) oxidization temperature at a fixed current density of 5 A/dm^2.

Fig. 2 The spectral reflectance plots versus (a) different current densities at 0 °C for 60 min, (b) different temperatures under 5 A/dm^2 for 60 min. (c) The SEM image of thermo-anodized surface at 8 °C. Solar absorptivity and emittances at (d) different current densities and (e) different anodizing temperatures. (f) absorptivity and emittance for the coatings versus coating thicknesses.
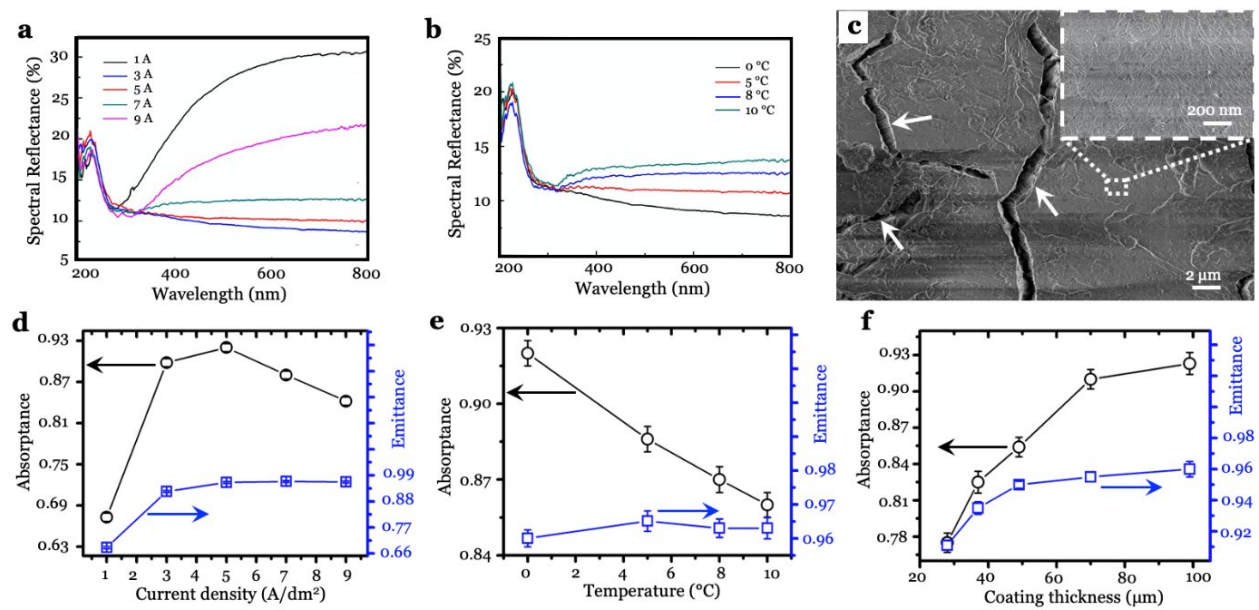
Fig. 3 Potentiodynamic polarization curves of coated aluminium alloys at 0 °C for 60 min under different current densities in 3.5% NaCl solution, (a) without UV irradiation, (b) under UV irradiation (400 nm). Potentiodynamic polarization curves of coated aluminium alloys at 5 A/dm2 for 60 min under different temperatures in 3.5% NaCl solution (c) without UV irradiation, (d) under UV irradiation (400 nm).

Fig. 4 (a) The schematic of fabricating hybrid hydrophobic surface by silanization. (b) SEM of hybrid AAO coatings by silanizing using KH-550 at 30°C. (c) The thickness and roughness of coatings after annealing at different temperatures. (d) The reflectance results of untreated coating and hybrid coatings at different temperatures. (e) absorptivity and emittance for the hybrid coatings annealed at different temperatures.
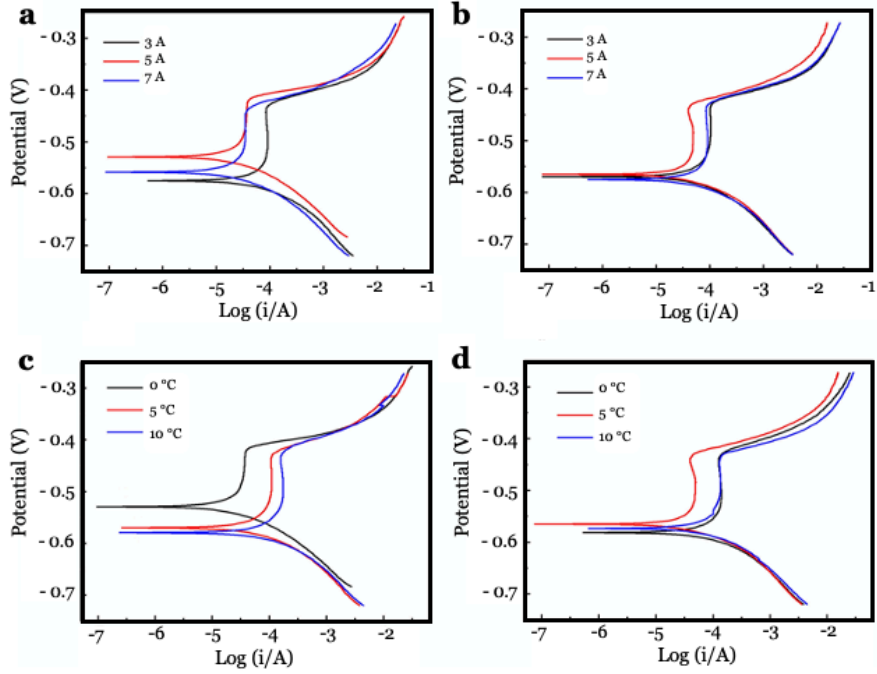
Fig. 5 Schematic illustration of the hydrophobic state in (a). Observations of contact angles for sample with (b) no seal and with AAO coatings annealed at (c) 20°C, (d) 30°C, (e) 40°C. (f) Summary of contact angles with contact angle hysteresis data. Observations of icing process of a single droplet of DI water on untreated CTC surface (g) liquid as deposited and (h) frozen state, and on hybrid surface with silane annealed at and 40 °C (i) liquid as deposited and (j) frozen state.
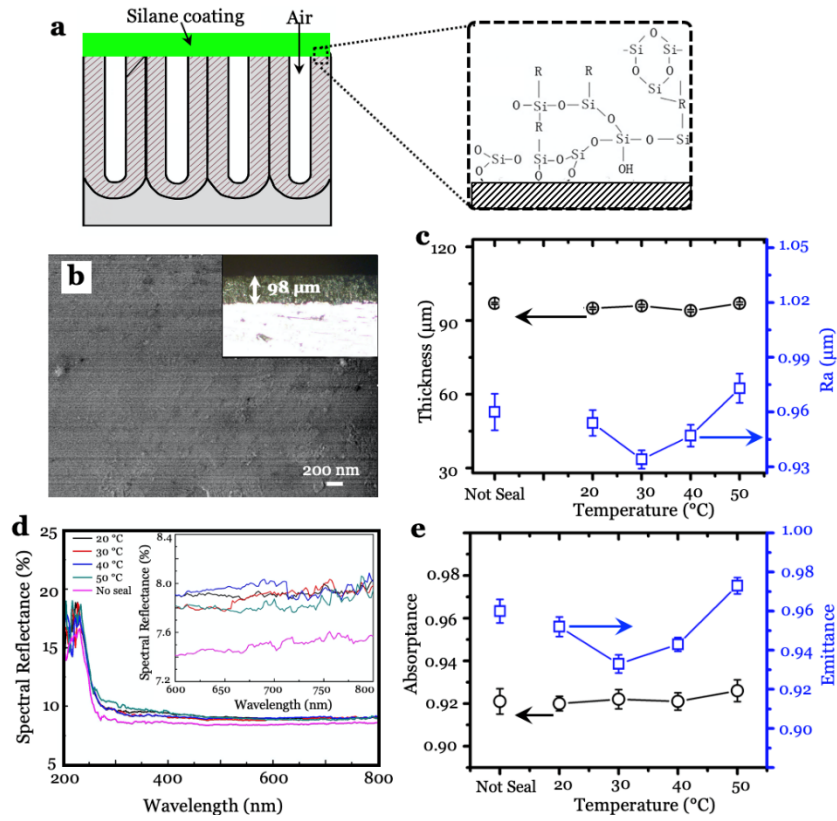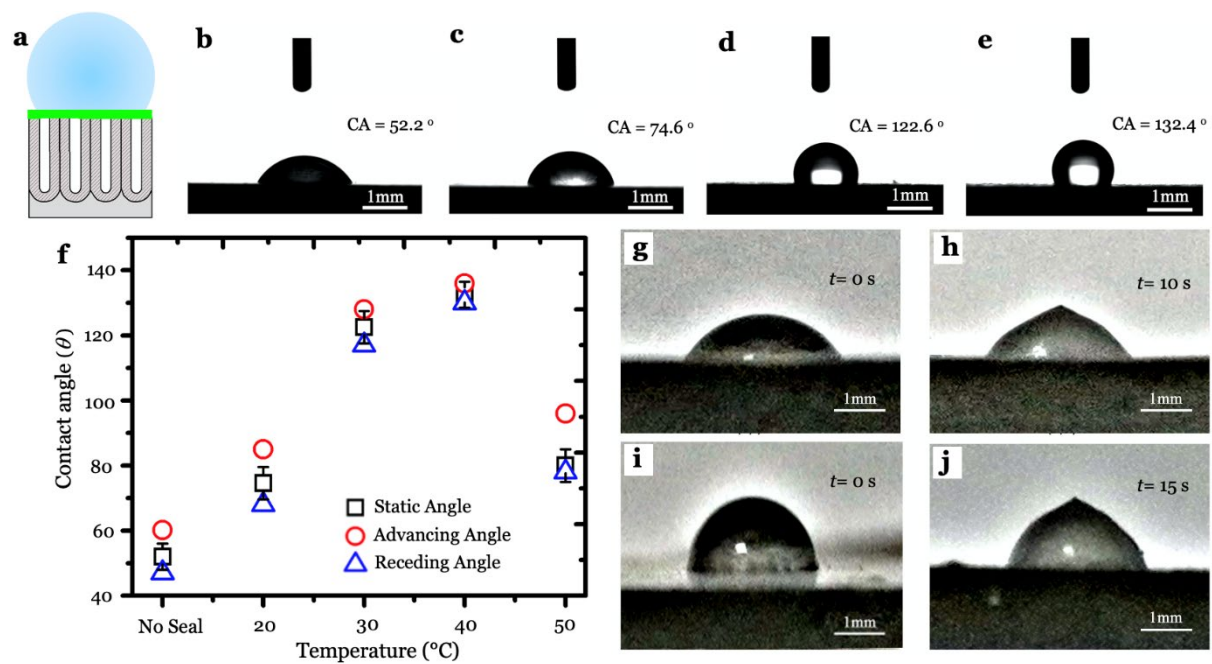
1

2

3

4

a

b   CA = 52.2 °   1mm

c   CA = 74.6 °   1mm

d   CA = 122.6 °   1mm

e   CA = 132.4 °   1mm

f

Contact angle (θ)

140
120
100
80
60
40

□ Static Angle
○ Advancing Angle
△ Receding Angle

No Seal   20   30   40   50

Temperature (°C)

g t = 0 s   1mm

h t = 10 s   1mm

i t = 0 s   1mm

j t = 15 s   1mm

5

Graphical Abstract

A Highly Controlled Fabrication of Porous Anodic Aluminium Oxide Surface with Versatile Features by Spatial Thermo-anodization

Zhehui Zhang[//], Sreepathy Sridhar[//], Guoying Wei*, Yundan Yu, Zhongquan Zhang, Li Jiang, Yumeng Yang, Muhammad Shahzad, Xue Chen, Ben B. Xu*

ToC Figure